A honeybee's navigational toolkit on Board a Bio-inspired Micro Flying Robot

Erik Vanhoutte, Franck Ruffier and Julien Serres *
Aix-Marseille Univ, CNRS, ISM, Marseille, France

http://www.imavs.org/

ABSTRACT

In this paper, a 395-gram micro flying robot equipped with an insect-inspired visual system is presented. The robot's visual system was designed to make it avoid both ground and lateral obstacles, using optic flow-based regulation principles. The quadrotor is an open-hardware X4-MaG drone with an active gimbal system based on a pair of serial servo motors, which stabilizes 8 retinas dedicated to optic flow measurements in the 25 $°/s$ to 1000 $°/s$ range, each of which comprises 12 auto-adaptive pixels working in a 7-decade lighting range. The X4-MaG drone is tested in front of a slanted wall, its quasi-panoramic bio-inspired eye on board is able to estimate the angle of incidence in the 0° to 50° range with an error of less than 2.5° when flying. These experimental results are a first step towards a fully autonomous micro quadrotor requiring no magnetometers, which will be able in the near future to "sense and avoid" obstacles in GPS-denied environments.

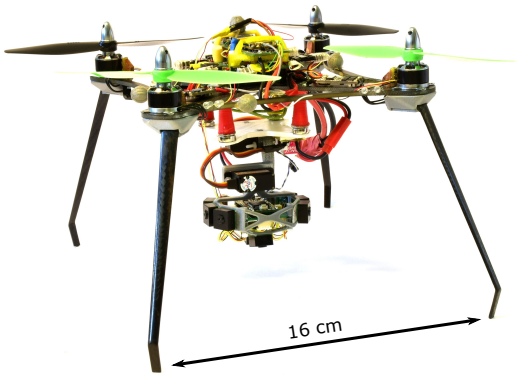

Figure 1: Photograph of the X4-MaG quadrotor with the gimbal case attached below (total mass: 395 g, span: 30 cm, autonomy: 6 min).

*Correspondance: julien.serres@univ-amu.fr; Tel.: +33(0)4 91 26 62 38

1 INTRODUCTION

Mimicking the flight of a tiny honeybee is still an arduous task [1, 2]. Since insect-sized micro air vehicles are increasingly becoming reality, however, [3, 4, 5, 6] it will be necessary to endow them in the future with sensors and flight control devices enabling them to perform all kinds of aerial maneuvers, including ground and obstacle avoidance, terrain-following and landing, in the same way as honeybees. This is a difficult challenge in the field of robotics, although drones can now be miniaturized thanks to recent advances in embedded electronics.

Stereovision-based strategies on board micro flying robots have recently provided means of exploring and avoiding obstacles indoors, but only under slow flight conditions [7, 8]. Micro LiDAR (Light Detection And Ranging devices) are also available for micro air vehicle applications (e.g., Centeye Inc. in the USA or LeddarTech Inc. in Canada), but these devices require a scanning system and have a high energy consumption. The optic flow (OF) is also a relevant visual cue which can be used for quickly sensing the configuration of the environment using either micro cameras or custom-made OF sensors.

Unfortunately, micro cameras sample tens of thousands of pixels with a refresh rate of only about 30 frames per second [9, 10], which is 10 times lower than the temporal resolution of the bees eye ($\sim$ 300 Hz, see [1]), and they also require much more computational resources than custom-made OF sensors. In addition, micro cameras are blinded by the changes in the light which occur when moving from one room to another, from indoor to outdoor conditions, or when encountering strong sunny to shadow contrasts. However, custom-made OF sensors lighten both the weight and the CPU load of micro flying robots , and enable them to make quasi panoramic OF measurements [11, 12, 13] as well as to work under various unpredictable lighting conditions. Because of their lack of visual stabilization, micro flying robots have to fly at low speeds despite the use of OF regulation principles [14, 10]. Up to now, no OF sensing strategies based on a stabilization system preventing the rotational effects have yet been implemented on board a micro flying robot.

In [9], the slope of the ground was assessed on board a quadrotor. In [15], 10 local OF measurements coupled to a least mean squares method were used to stabilize a minimalistic quasi-panoramic compound eye on the Beerotor robot with respect to the local downward slope, thus enabling the robot to avoid any very steep relief encountered. In [16], an

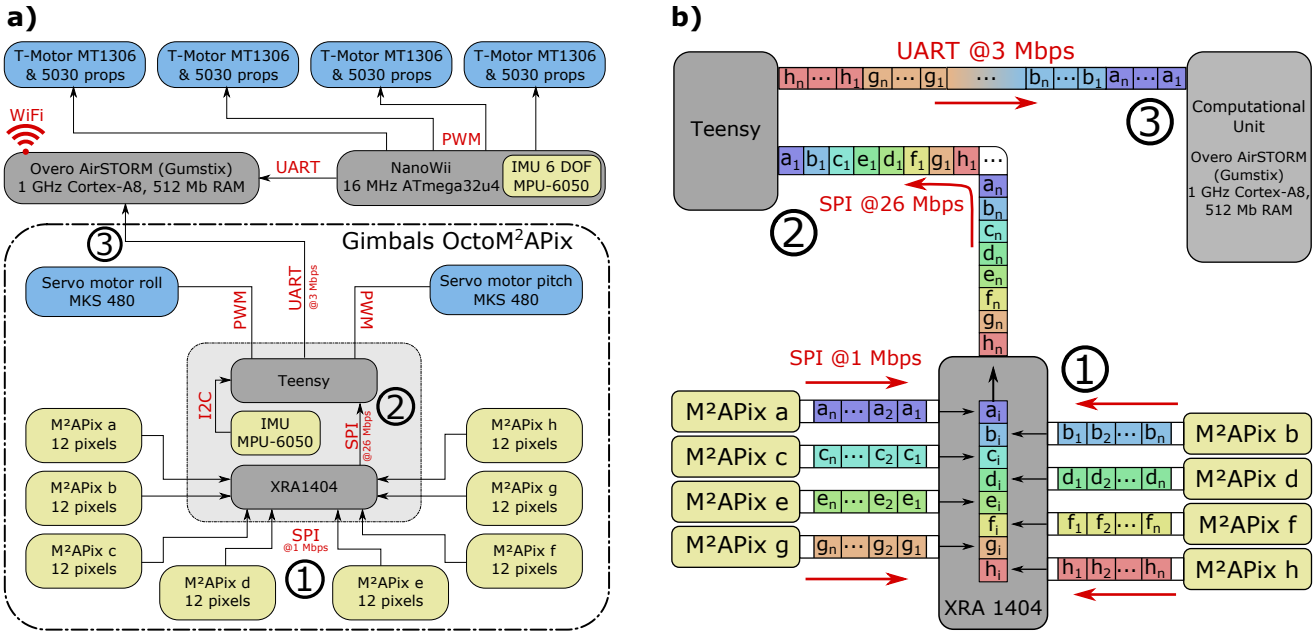

Figure 2: a) Component architecture of the X4-MaG quadrotor with the gimbal elements surrounded by a dash-dot line. The development boards and the data transmission units are shown in gray, the actuators in blue, and the sensors in yellow. b) Data diagram of how visual signals originating from the OctoM^{2}APix eye are processed: ① high speed synchronous data capture, ② data put in order, and ③ signal processing for optic flow computations.

innovative OF-based algorithm was tested in the horizontal plane as a means of measuring the robot's incidence angle when perceiving a slanting wall showing a moving texture. The results of our experiments showed that our minimalistic algorithm based on 20 local OF measurements could be used to determine the local visual heading with respect to the moving slanting wall with an error of less than 3° and a mean accuracy of 3° [16].

In the present paper, a bio-inspired micro flying robot, which will be able to perform both wall-following and ground-avoidance tasks in GPS-denied (Global Positioning System-denied) environments. This robot is fitted with a visual stabilization system involving 8 custom-made OF sensors which can respond appropriately in a 7-decade lighting range [17] and can measure the OF magnitude from 25 $^\circ/s$ to 1000 $^\circ/s$ [18]. It was established in real flight tests that this micro flying robot is able to estimate its incidence angle with respect to a slanting wall in order to restore its flight parallel to the wall. The results obtained in the present study show that our quasi-panoramic bio-inspired eye coupled to a computational unit can estimate this incidence angle in the 0° to 50° range when flying.

2 MICRO FLYING ROBOT

The micro flying robot presented here, a 320-gram quadrotor that can carry a maximum payload of 90 g, is based on the open-hardware X4-MaG model [19]. Thanks to an open-source Matlab/Simulink toolbox [20], it is possible to monitor this quadrotor in real time by wifi and change the relevant parameters directly during its flight. We have added to this quadrotor a custom-made 3D print gimbal case endowed with a magnet-based system of fixation facilitating its removal. This custom-made gimbal stabilizes the 8 OF sensors on the pitch and roll axes via two 10-gram serial servo motors (Fig. 1). The first group of 3 OF sensors oriented to the left measure a left OF, the second group of 3 sensors oriented to the right measure a right OF: each of these groups has a field of view of 92.8° in the horizontal plane and 13.4° in the vertical plane. The third group of two downward-oriented sensors measure the ventral OF with a field of view of 62.8° in the forward axis and 13.4° in the orthogonal axis. The gimbal system, which is stabilised in attitude during the robot's flight, has a total mass of 75 grams enabling the robot to fly for 6 minutes.

The quadrotor is fitted with a low-level autopilot based on the Nanowii (ATmega32u4, MultiWii) with a 6 degrees of freedom Inertial Measurement Unit (IMU) (Fig. 2a). This low-level control board makes it possible for the robot to be piloted manually and takes over from the Gumstix if failure of the latter occurs. All attitude and trajectory control processes based on the OF measurements are handled by the high-level autopilot based on an Overo AirSTORM Computer-On-Module (COM) (*Gumstix*) featuring a 1-GHz CPU DM3703 processor (*Texas Instruments*) comprising an ARM Cortex-A8 architecture. A Teensy 3.2 featuring a 72 MHz Cortex-M4 (PJRC) controls the gimbal servo motors and also reads

http://www.imavs.org/

http://www.imavs.org/

the 8 retinas (dedicated to OF measurements) and transmits the pixel data to the Overo AirSTORM (Fig. 2a, for details).

3 OPTIC FLOW SENSORS

The M^{2}APix sensor is a bio-inspired OF sensor based on a Michaelis-Menten Auto-adaptive Pixel analog silicon retina that can auto-adapt in a 7-decade lighting range and responds appropriately to stepwise changes of up to $\pm$ 3 decades [17]. Each M^{2}APix sensor is composed of 12 pixels distributed in two rows of six pixels offset by half the interpixel distance [17], and is able to make 10 local OF measurements with a high output refresh rate [18]. The local OF is measured using a time-of-travel algorithm based on a contrast detection matching method (called the thresholding method) running at only 1 kHz along the pixels rows axis.

The CPU load of the Overo AirSTORM is less than 3 percent per M^{2}APix sensor and the OF refresh rate is up to 99 Hz per M^{2}APix sensor with an OF ranging from 25 $^\circ/s$ to 1000 $^\circ/s$ [18].

4 A GIMBAL SYSTEM NAMED OCTOM^{2}APIX

A custom-made PCB was designed for the gimbal system named OctoM^{2}APixto connect the following components (Fig. 2a): a Teensy 3.2 featuring a 72 MHz Cortex-M4 (PJRC), an 8-bit SPI GPIO EXPANDER called XRA1404 (Exar©), an Inertial Measurement Unit (IMU) MPU 6050, and connections to 8 M^{2}APix sensors and 2 servo motors belonging to the gimbal system, in order to stabilize the bio-inspired eye on the pitch and roll axes and thus remove any rotational OF components.

A M^{2}APix sensor works with a SPI bus running at a maximum rate of 1 MHz, which transmits a 256-bit data frame, and the maximum theoretical frame rate is therefore 3906 Hz. SPI devices communicate in the full duplex mode using a master-slave architecture with a single master. Only one SPI bus is usually available on dedicated electronic boards. The maximum frame rate possible to obtain data from the 8 slave M^{2}APix sensors is therefore less than 488 Hz, and the data will not be processed synchronously but sequentially (Fig. 2b). To give from the 8 M^{2}APix sensors higher frame rates and make the processing synchronous, a XRA1404 GPIO EXPANDER was used. The XRA1404 can read the logic state on 8 digital ports and send this data as a byte to an SPI bus working at a frequency of 26 MHz (Fig. 2b). Each of these 8 digital ports is used to read the bit to bit data frame of each M^{2}APix sensor (step ① in the Fig. 2b). As a result, the first bit in all the M^{2}APix data frames are arranged in one byte, which is sent on to the SPI bus. Each bit in each M^{2}APix sensor is processed in this way.

The Teensy electronic board reads the SPI bus at a frequency of 26 MHz from the XRA1404 and puts each data frame of each M^{2}APix sensor back into order (step ② in Fig. 2b). The M^{2}APix sensor sends a mean light value and 12 pixel values, each of which is coded in 10-bit values. The algorithm then selects only the pixel data. This leaves us with 12x10 bits per M^{2}APix sensor. Lastly, the Teensy removes the offset of the range used and deletes the last bit which is equivalent to the amplitude of the noise, to express the data in the 8-bit format. The 12 pixels coded with the 8-bit value of the 8 M^{2}APix sensors are then sent to the serial bus at a speed of 3 Mbps to a computational unit to compute the OF (step ③ shown in Fig. 2b).

5 FLYING STRATEGIES

The OctoM^{2}APix is designed to make the X4-MaG drone both follow walls and adjust its height at relatively high speeds (up to 2.5 $m \cdot s^{-1}$) by removing the rotational OF component of the sensing performed by the 8 M^{2}APix sensors. Wall-following and ground-following behaviour will be obtained by merging OF regulation principles [21]. The aim of the flying strategies we propose to pursue in the near future will be to maintain the visual contact with the walls in order to make the robot fly in parallel along one of them. These strategies will involve adding another visual feedback loop controlling the yaw component by estimating the relative local angle between the nearest wall (e.g., the red rectangle in Fig. 4a) and the flying robot. Figure 3 and Eq. 1 explain how to obtain this incidence angle α from OF measurements with a very light solution in terms of the computational resources required, where c is cos, s is sin, and t is the tan function.

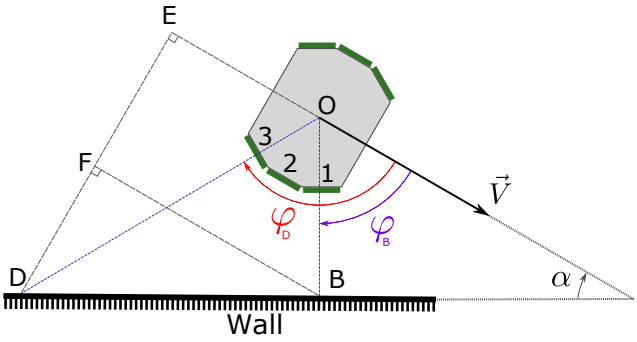

Figure 3: Geometry of the OctoM^{2}APix eye (centring in O) on the horizontal plane with a tapered wall on its left-hand side. Each green rectangle represents one M^{2}APix sensor. In the left-hand side, the M^{2}APix are numbered to make the experiments easier to understand.

$$\omega_B = \frac{V}{OB} \cdot s(\varphi_B) \qquad \omega_D = \frac{V}{OD} \cdot s(\varphi_D)$$

$$t(\alpha) = \frac{OD \cdot s(\varphi_D) - OB \cdot s(\varphi_B)}{OB \cdot c(\varphi_D) - OD \cdot c(\varphi_B)}$$

$$t(\alpha) = \frac{\frac{1}{\omega_D} \cdot s(\varphi_D)^2 - \frac{1}{\omega_B} \cdot s(\varphi_B)^2}{\frac{1}{\omega_B} \cdot s(\varphi_B) \cdot c(\varphi_B) - \frac{1}{\omega_D} \cdot s(\varphi_D) \cdot c(\varphi_D)}$$

$$\alpha = t^{-1}\left(\frac{\omega_B \cdot s(\varphi_D)^2 - \omega_D \cdot s(\varphi_B)^2}{\omega_D \cdot s(\varphi_B) \cdot c(\varphi_B) - \omega_B \cdot s(\varphi_D) \cdot c(\varphi_D)}\right) \quad (1)$$

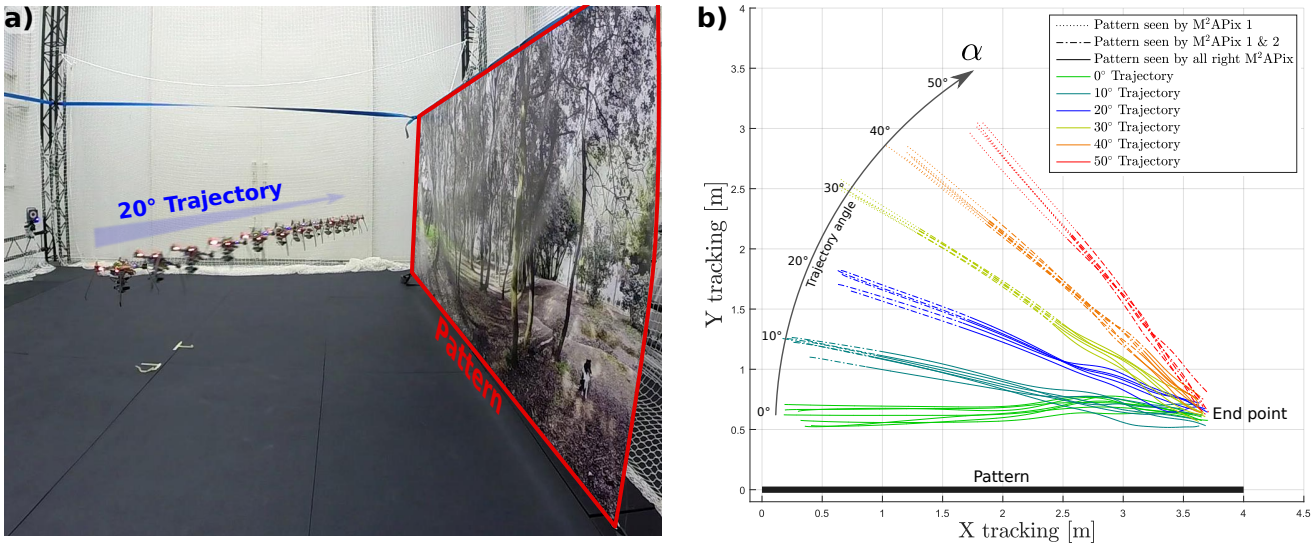

Figure 4: a) Chronophotograph of the X4-MaG drone at the Mediterranean Flying Arena. The flying robot followed a textured "wall" sloping at an angle of 20° for about 4.5 s (corresponding to one of the blue trajectories in b). b) Top view of all the trajectories taken in the Mediterranean Flying Arena[1]. 6 different trajectories were tested at the same height (0.8 $m \pm 0.01$ m) with a clockwise angle between the trajectories and the patterned wall. The X4-MaG drone followed each trajectory several times. Depending on the angle of the trajectory, either M^{2}APix #3 or both M^{2}APix #2 & #3 did not perceive the pattern on the wall due to their orientation (their positions are given by a dashed line and a dotted line, respectively).

6 FLYING EXPERIMENT

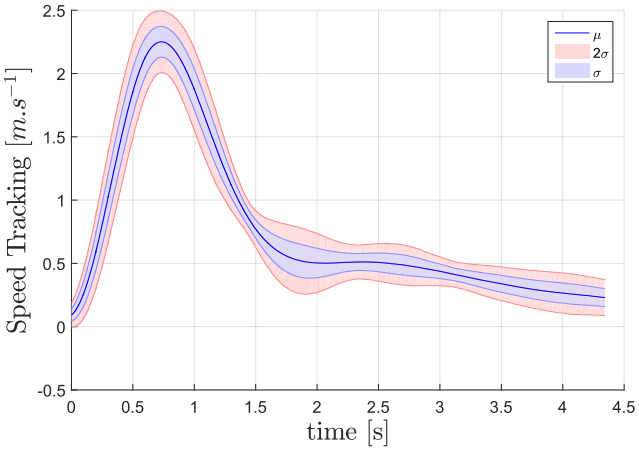

Figure 5: Speed profile (in XY plane) of the aerial robot for all the trajectories presented in Fig. 4b. μ is the mean value and σ is the standard deviation.

This flight experiment consisted in observing the dynamic responses of the OctoM^{2}APix sensor with all the components integrated during real flight. The X4-MaG flying at the Mediterranean Flying Arena[1] (6x8x6 m): its trajectory was controlled in the closed loop mode with a motion capture system (VICON^{TM}). A 4-m long wall covered with a natural pattern was hanging in the arena to generate OF when the X4-MaG approached it. The X4-MaG repeated various straight trajectories 6 times at the same height (0.8 $m \pm 0.01$ m) with the pattern on the right-hand side and with an angle of incidence α between its trajectory and the pattern ranging from 0° to 50° in 10° steps (Fig. 4). The three M^{2}APix sensors could therefore potentially detect the pattern and measure the OF during the experiments.

To test the case of future aggressive maneuvers in an indoor environment, the flights were then performed at high speed (up to 2.5 $m \cdot s^{-1}$, see Fig. 5) near obstacles (with a clearance of up to 0.5 m, see Fig. 4). The figure 5 gives the speed profiles of all the trajectories including one high acceleration (up to 6 $m \cdot s^{-2}$) phase and one high deceleration phase.

The figure 4b presents all the trajectories tracked. Due to the flying robots proximity with the patterned wall, aerodynamic perturbations were generated at the end of the trajectories, during the last metre (Fig. 4b). During a part of the trajectories from 10° to 50° shown by a dashed line, the pattern was not visible to the M^{2}APix #3 (oriented at an angle of 120° in Fig. 3) , and the dotted lines indicate the part of the trajectories where the pattern was not visible to the M^{2}APix #2 (oriented at an angle of 90° in Fig. 3). None of the OF measurements obtained during these dashed and dotted parts of the trajectories were included in the following statistical analyses.

A median filter was applied to the 10 local OF measurements obtained by each M^{2}APix sensor, and the M^{2}APix out-

[1] http://flying-arena.eu/

http://www.imavs.org/

http://www.imavs.org/

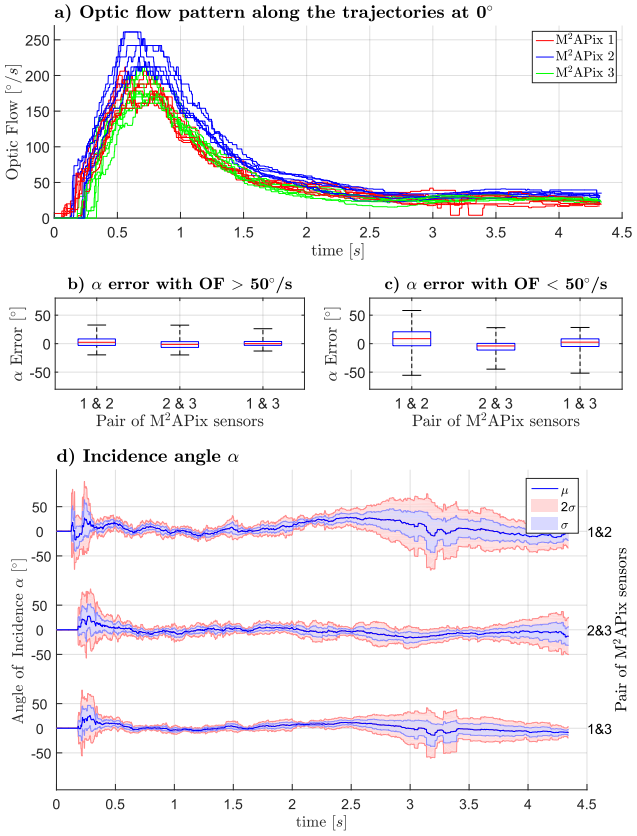

Figure 6: a) Optic flow measurements of M^{2}APix #1 (red), #2 (blue) & #3 (green), during all the trajectories performed at 0°. b) and c) Errors distribution of the angles of incidence α per pair of M^{2}APix sensors when all the optic flow measurements were greater than $50°/s$ in c), and less than $50°/s$ in d), where the red bar is the median, the black whiskers correspond to min and max values, and the blue box is the interquartile range (IQR) at 50 %. b) median $\pm$ IQR obtained for pair #1&#2 : $2.4° \pm 11.4°$; pair #2&#3 : $-1.2° \pm 10.1°$; pair #1&#3 : $0.0° \pm 6.8°$. c) median $\pm$ IQR for pair #1&#2 : $8.8° \pm 24.5°$; pair #2&#3 : $-4.0° \pm 11.7°$; pair #1&#3 : $2.6° \pm 13.4°$. d) Angle of incidence α computed for each pair of M^{2}APix sensors. μ is the mean value and σ is the standard deviation.

puts were then used in pairs to compute Eq. 1 in order to estimate the local angle of incidence α (Fig. 3). We thus obtained 3 measurements of the α angle from these pairs (#1&#2, #2&#3 and #1&#3). Statistical results of the angular measurements obtained from each set of trajectories (from 0° to 50°) are presented in Figs. 6 to 11 in 10° steps.

The optical parameters of the M^{2}APix sensors were chosen so as to be able to measure OF values greater than 50° /s (up to $1000°/s$, see [18]) accurately. The angle of incidence α was therefore estimated more accurately with OF values greater than 50° /s, as shown in Figs. 6b-11b than in Figs 6c-11c. The lowest α errors were consistently obtained with the pair of M^{2}APix sensors #1 and #2 (Figs. 6b,c-11b,c), where

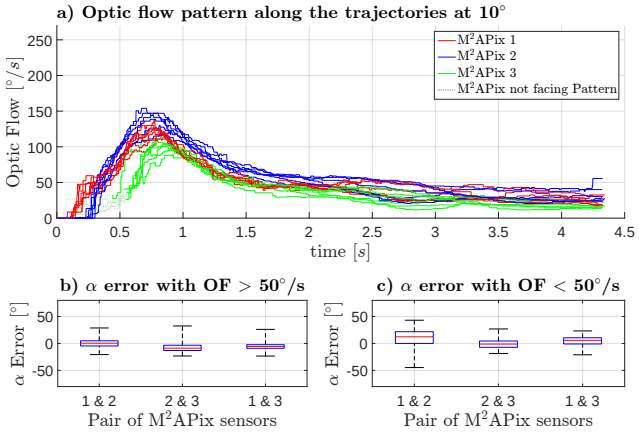

Figure 7: a) Optic flow measurements made by M^{2}APix #1 (red), #2 (blue) & #3 (green) during all the trajectories performed at 10°. b) c) Errors distribution of the angles of incidence α recorded per pair of M^{2}APix when all the optic flow measurements were greater than $50°/s$ in b) and less than $50°/s$ in c), where the red bar is the median, the whiskers correspond to min and max values and the blue box is the IQR at 50 %. OF measurements plotted in dotted lines were not generated by the pattern on the wall and were therefore not included in the results presented in b) and c) in this figure and the next ones. b) median $\pm$ IQR for pair #1&#2 : $0.5° \pm 9.6°$; pair #2&#3 : $-8.7° \pm 9.8°$; for pair #1&#3 : $-5.6° \pm 6.7°$. c) median $\pm$ IQR for pair #1&#2 : $12.3° \pm 21.8°$; pair #2&#3 : $-1.2° \pm 11.7°$; pair #1&#3 : $5.7° \pm 11.5°$.

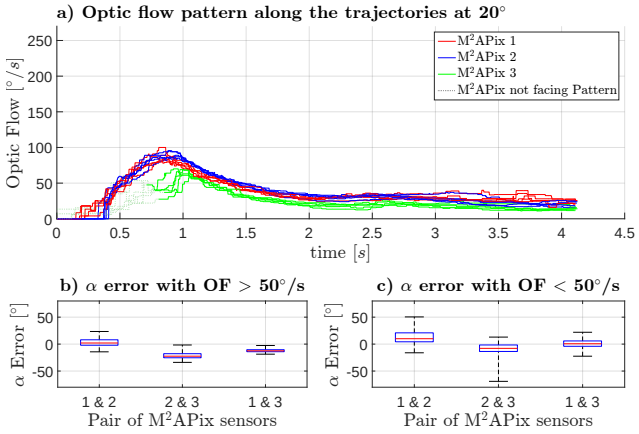

Figure 8: Results obtained on the trajectories at 20°. b) median $\pm$ IQR for pair #1&#2 : $2.0° \pm 10.1°$; for pair #2&#3 : $-22.4° \pm 7.6°$; pair #1&#3 : $-12.5° \pm 3.7°$. c) median $\pm$ IQR for pair #1&#2 : $10° \pm 16.6°$; pair #2&#3 : $-7.9° \pm 12.0°$; pair #1&#3 : $0.6° \pm 9.9°$.

the median error was less than 2.5°. This pair of sensors was that which was the most oriented towards the frontal part of the OF field.

The visual strategy developed in this study should therefore be consistent with the confidence range of the angle of incidence α estimated when the OF values measured on the

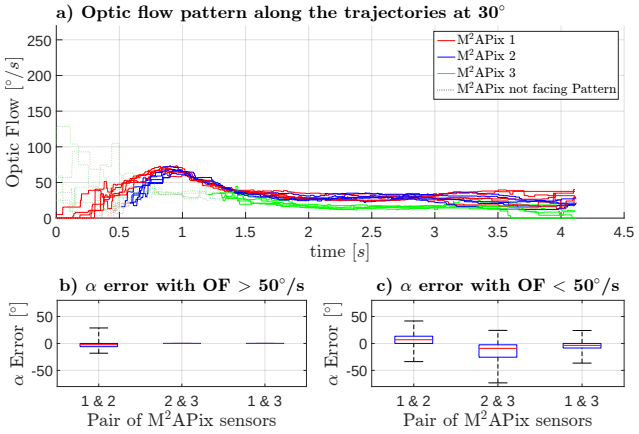

Figure 9: Results obtained on the trajectories 30°. The M²APix 3 did not measure optic flows greater than $50°/s$, which explains the lack of results on the pair of M²APix #2&#3 and #1&#3 in b). b) median ± IQR for pair #1&#2 : $-2.3° \pm 6.0°$. c) median ± IQR for pair #1&#2 : $6.9° \pm 13.4°$; pair #2&#3 : $-9.1° \pm 23.0°$; pair #1&#3 : $-3.5° \pm 8.5°$.

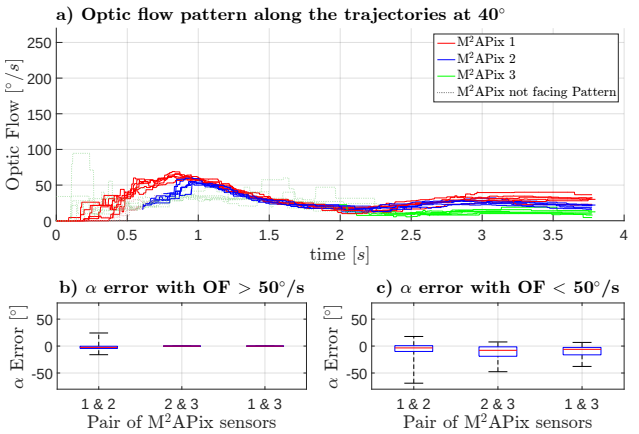

Figure 10: Results obtained on the trajectories 40°. b) median ± IQR for pair #1&#2 : $-2.5° \pm 4.1°$. c) median ± IQR for pair #1&#2 : $-3.4° \pm 10.7°$; pair #2&#3 : $-7.9° \pm 17.5°$; pair #1&#3 : $-6.0° \pm 13.8°$.

micro aerial vehicle were high, i.e. at high speeds, as well as when the micro aerial vehicle was travelling very near the walls.

7 CONCLUSION

The 395-gram X4-MaG quadrotor fitted with a gimbal system and a set of 8 custom-made optic flow sensors provides an appropriate flying platform for testing optic-flow regulation principles during real flight with a view to mimicking honeybees' flight performances. The gimbal system makes it possible to minimize the effects of the rotational component of the optic flow measured by the quasi-panoramic bio-inspired eye. The results obtained in these experiments show that our optic flow based algorithm can estimate the drone's local angle of incidence with respect to a slanting wall in the 0° to 50° range during flight with an error of less than 2.5°, using the optic flow generated on either side (left or right). To measure larger angles of incidence (from 50° to 90°), the fronto-bilateral optic flow could be used in the similar way to that simulated in [22], but this possibility is beyond the scope of the present study and would require measuring the low optic flow values occurring close to the focus of expansion.

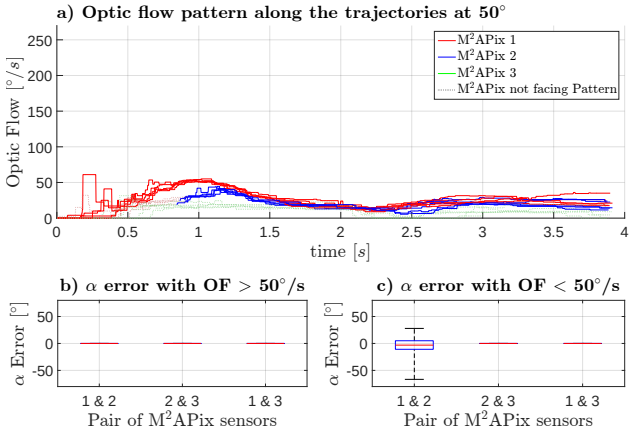

Figure 11: Results obtained on the trajectories at 50°. The pattern on the wall was not visible to M²APix #3 during all these trajectories, which explains the lack of data on the pair of M²APix #2&#3 and #1&#3 in c). c) median ± IQR for pair #1&#2 : $-3.1° \pm 15.8°$.

In the near future, flying at high speed (up to 1 m/s) near obstacles (at a distance of less than 0.5 m) may be possible thanks to the large range of optic flow measurements which can now be made, namely up to $1000°/s$. The advantages of the custom-made optic flow sensors used here include low power consumption, low computational requirements, and robustness to high dynamic range lighting conditions (7 decades). In conclusion, the present X4-MaG drone fitted with smart visual sensors is the first step towards designing airborne vehicles capable of autonomous navigation requiring no magnetometers in GPS-denied environments.

ACKNOWLEDGEMENTS

We thank J. Diperi for the mechanical design of the flying robot and the test bench, M. Boyron for his involvement in the overall electronic design of the flying robot, and K. Contamain, S. Mafrica, and F. Colonnier for their help with both the electronic development and the programming of the M²APix sensors. This research was supported by the French Direction Générale de l'Armement (DGA), CNRS, Aix-Marseille Université, the Provence-Alpes-Côte d'Azur region and the French National Research Agency for Research (ANR) in the framework of the Equipex/Robotex project.

http://www.imavs.org/

http://www.imavs.org/

REFERENCES

[1] M. V. Srinivasan, "Honeybees as a model for the study of visually guided flight, navigation, and biologically inspired robotics," *Physiological reviews*, vol. 91, no. 2, pp. 413–460, 2011.

[2] J. R. Serres and F. Ruffier, "Optic flow-based collision-free strategies: From insects to robots," *Arthropod Structure & Development*, 2017 (in press).

[3] P.-E. J. Duhamel, N. O. Pérez-Arancibia, G. L. Barrows, and R. J. Wood, "Altitude feedback control of a flapping-wing microrobot using an on-board biologically inspired optical flow sensor," in *Robotics and Automation (ICRA), 2012 IEEE International Conference on*, pp. 4228–4235, IEEE, 2012.

[4] A. Kushleyev, D. Mellinger, C. Powers, and V. Kumar, "Towards a swarm of agile micro quadrotors," *Autonomous Robots*, vol. 35, no. 4, pp. 287–300, 2013.

[5] K. Y. Ma, P. Chirarattananon, S. B. Fuller, and R. J. Wood, "Controlled flight of a biologically inspired, insect-scale robot," *Science*, vol. 340, no. 6132, pp. 603–607, 2013.

[6] O. Dunkley, J. Engel, J. Sturm, and D. Cremers, "Visual-inertial navigation for a camera-equipped 25g nano-quadrotor," in *IROS2014 aerial open source robotics workshop*, 2014.

[7] K. McGuire, G. de Croon, C. De Wagter, K. Tuyls, and H. Kappen, "Efficient optical flow and stereo vision for velocity estimation and obstacle avoidance on an autonomous pocket drone," *IEEE Robotics and Automation Letters*, vol. 2, no. 2, pp. 1070–1076, 2017.

[8] Centeye, *Centeye nano unmanned aircraft system with 360-degree stereo vision*. Washington, DC: http://www.centeye.com/small-nano-uas-autonomy, 2016.

[9] G. De Croon, H. Ho, C. De Wagter, E. Van Kampen, B. Remes, and Q. Chu, "Optic-flow based slope estimation for autonomous landing," *International Journal of Micro Air Vehicles*, vol. 5, no. 4, pp. 287–297, 2013.

[10] C. Sabo, E. Yavuz, A. Cope, K. Gumey, E. Vasilaki, T. Nowotny, and J. A. Marshall, "An inexpensive flying robot design for embodied robotics research," in *Neural Networks (IJCNN), 2017 International Joint Conference on*, pp. 4171–4178, IEEE, 2017.

[11] J. Keshavan, G. Gremillion, H. Alvarez-Escobar, and J. S. Humbert, "Autonomous vision-based navigation of a quadrotor in corridor-like environments," *International Journal of Micro Air Vehicles*, vol. 7, no. 2, pp. 111–123, 2015.

[12] R. J. Moore, K. Dantu, G. L. Barrows, and R. Nagpal, "Autonomous mav guidance with a lightweight omnidirectional vision sensor," in *2014 IEEE International Conference on Robotics and Automation (ICRA)*, pp. 3856–3861, IEEE, 2014.

[13] A. Briod, J.-C. Zufferey, and D. Floreano, "A method for ego-motion estimation in micro-hovering platforms flying in very cluttered environments," *Autonomous Robots*, vol. 40, no. 5, pp. 789–803, 2016.

[14] C. Sabo, A. Cope, K. Gurny, E. Vasilaki, and J. A. R. Marshall, "Bio-Inspired Visual Navigation for a Quadcopter using Optic Flow," *AIAA Infotech @ Aerospace*, no. January, pp. AIAA 2016–0404, 2016.

[15] F. Expert and F. Ruffier, "Flying over uneven moving terrain based on optic-flow cues without any need for reference frames or accelerometers," *Bioinspiration and Biomimetics*, vol. 10, 2015.

[16] E. Vanhoutte, F. Ruffier, and J. Serres, "A quasi-panoramic bio-inspired eye for flying parallel to walls," in *Sensors, 2017 IEEE*, (paper 1332, Glasgow, Scotland, UK), IEEE, 2017 (in press).

[17] S. Mafrica, S. Godiot, M. Menouni, M. Boyron, F. Expert, R. Juston, N. Marchand, F. Ruffier, and S. Viollet, "A bio-inspired analog silicon retina with Michaelis-Menten auto-adaptive pixels sensitive to small and large changes in light," *Optics Express*, vol. 23, no. 5, p. 5614, 2015.

[18] E. Vanhoutte, S. Mafrica, F. Ruffier, R. Bootsma, and J. Serres, "Time-of-Travel Methods for Measuring Optical Flow on Board a Micro Flying Robot," *Sensors*, vol. 17, no. 3, p. 571, 2017.

[19] A. Manecy, N. Marchand, F. Ruffier, and S. Viollet, "X4-MaG : A Low-Cost Open-Source Micro-Quadrotor and Its Linux-Based Controller," *International Journal of Micro Air Vehicles*, vol. 7, no. 2, pp. 89–110, 2015.

[20] A. Manecy, N. Marchand, and S. Viollet, "RT-MaG: An open-source SIMULINK toolbox for Linux-based real-time robotic applications, year=2014, pages=173-180, doi=10.1109/ROBIO.2014.7090326, month=Dec,"

[21] G. Portelli, J. Serres, F. Ruffier, and N. Franceschini, "Modelling honeybee visual guidance in a 3-D environment," *Journal of Physiology Paris*, vol. 104, no. 1-2, pp. 27–39, 2010.

[22] J. R. Serres and F. Ruffier, "Biomimetic autopilot based on minimalistic motion vision for navigating along corridors comprising u-shaped and s-shaped turns," *Journal of Bionic Engineering*, vol. 12, no. 1, pp. 47–60, 2015.